

# A Novel Vessel Segmentation Algorithm for Pathological Retina Images Based on the Divergence of Vector Fields

Benson Shu Yan Lam\* and Hong Yan

**Abstract**—In this paper, a method is proposed for detecting blood vessels in pathological retina images. In the proposed method, blood vessel-like objects are extracted using the Laplacian operator and noisy objects are pruned according to the centerlines, which are detected using the normalized gradient vector field. The method has been tested with all the pathological retina images in the publicly available STARE database. Experiment results show that the method can avoid detecting false vessels in pathological regions and can produce reliable results for healthy regions.

**Index Terms**—Blood vessel segmentation, gradient vector field, image segmentation, retina image analysis.

## I. INTRODUCTION

IN retinal images, blood vessels are landmarks for localizing the optic nerve, the fovea and lesions, which are useful for medical diagnosis. However, in these images, many vessels are narrow and close to each other, forming a network-like structure. Also, due to the reflection on the tiny uneven surface of the soft tissue in the image, the low contrast between the vessel and background, and the pathological variations, detecting blood vessels automatically from a retinal image is a challenging problem. A number of techniques have been proposed to solve this problem. They can be classified into unsupervised and supervised methods. In an unsupervised method, a pixel is assigned to a candidate vessel according to several predefined criteria. Chaudhuri *et al.* propose a matched filter response (MFR) method [1], which applies rotated Gaussian filters to the image. If the pixel has a large filtered value, it is a part of a vessel. Jiang and Mojon propose an adaptive thresholding technique for vessel segmentation [2]. The detection is conducted in different levels of image intensities. For example, the pixels with intensity values from 80 to 100 are grouped into one level while the pixels with the intensity values from 110

to 140 are grouped into another level. In each level, candidate vessels are obtained by thresholding. In a supervised method, the criteria are determined by the ground truth data based on given features. However, a prerequisite for a supervised method is the availability of the ground truth data that are already classified, which may not be available in real life applications. An average of 2 h is needed to label a single retinal image [3]. Staal *et al.* employ more than 10 features, including width of the vessel, intensity, and edge strength [3]. Soares *et al.* make use of the Gabor wavelet transform [4]. As supervised methods are designed based on preclassified data, their performance is usually better than that of unsupervised ones and can produce very good results for healthy retinal images.

Although existing methods are robust for many retinal images, there is still room for further improvement, especially for pathological retina images. A pathological retina may suffer from a certain disease and there may contain some spots (light or dark). Existing methods may recognize those spots as part of the vessels. Due to the unknown characteristics of a pathological region, widely used features such as intensity are not effective for solving the problem. The supervised method of Soares *et al.* has the same limitation. In their paper, the authors stated “Though very good ROC results are presented, visual inspection shows some typical difficulties of the method that must be solved by future work. The major errors are in false detection of noise and other artifacts. False detection occurs in some images for the border of the optic disc, haemorrhages, and other types of pathologies that present strong contrast” [4].

Researchers have made many proposals to analyze pathological retina images. Chanwimaluang *et al.* suggest that more constraints should be added in order to remove the spots [5]. However, there is no discussion on how we can select the constraints. One of the widely used constraints for noise removal is the split-and-merge system [6]. If the size of an object is small enough, it will be treated as noise. An implicit assumption for this pruning operation is that the size of the vessel should be larger than that of noise. However, many blood vessels after splitting are very short and can be removed easily. Staal *et al.* suggest to solve the problem by removing a pathological region in a preprocessing step or by selecting more training data sets that include pathological features in a supervised approach [3]. The removal of a pathological region in a preprocessing step can be difficult. Actually, as we do not know where a pathological region will be, it is not easy to remove it in advance. One way is to use an adaptive thresholding technique proposed by Jiang and Mojon [2]. They separate the image into several levels by

Manuscript received June 4, 2007; revised September 14, 2007. This work was supported by the City University of Hong Kong under Project 9610034. Asterisk indicates corresponding author.

\*B. S. Y. Lam is with the Department of Electronic Engineering, City University of Hong Kong, Kowloon, Hong Kong (e-mail: 50005347@student.cityu.edu.hk).

H. Yan is with the Department of Electronic Engineering, City University of Hong Kong, Kowloon, Hong Kong and with the School of Electrical and Information Engineering, University of Sydney, Sydney, NSW 2006, Australia (e-mail: h.yan@cityu.edu.hk).

Color versions of one or more of the figures in this paper are available online at <http://ieeexplore.ieee.org>.

Digital Object Identifier 10.1109/TMI.2007.909827

a thresholding method based on pixel intensities. However, if there are large intensity variations within the spots, this method may not work well. To produce more training data, one possible solution is to trace the vessels from the optic nerve, a user-defined point or a given labeled vessel on the image [7]–[15]. However, if the spots are close to the blood vessels, which are not connected to the optic nerve or the given information, it may not be possible to remove them.

Based on the above discussions, there is a clear need for a new approach to detect vessels in pathological retina images. In this paper, we propose a new method to solve this problem, especially for those pathological retina images containing bright abnormality. In our previous study, we proposed a partial differential equation based approach [16]. Partial differential equations have been widely used in many image processing problems including segmentation and inpainting [17]–[21]. This method is robust for healthy retinal images, but it is not so for pathological retina images. The method presented in this paper is an extension of our preliminary work in [16]. In the proposed method, blood vessel-like objects are extracted using the Laplacian operator and noisy objects are pruned according to the centerlines, which are detected using the normalized gradient vector field. Experiment results show that the proposed method is able to avoid detecting false vessels in pathological regions and can produce reliable results for healthy regions.

The organization of the paper is as follows. In Section II, we review the divergence operator. The concept of the proposed method is presented in Section III. In Section IV, we show the implementation details for each step. The robustness of the proposed method is shown by experiments in Section V. Finally, discussions and conclusions are given in Section VI.

## II. REVIEW OF DIVERGENCE OPERATOR

The divergence of the vector field has been widely used in fluid dynamics and electrodynamics [22], [23]. The definition of divergence of a vector field  $\mathbf{v}$  at point  $(x, y)$  is given below [24]

$$\nabla \cdot \mathbf{v}(x, y) = \lim_{r \rightarrow 0} \frac{1}{V_r} \iint_{S_r} \mathbf{v} \cdot \mathbf{n} d\rho \quad (1)$$

where  $V_r$  is the volume of the sphere  $\Omega_r$ ,  $S_r$  is the surface, and  $\mathbf{n}$  is the outward unit normal vector of the surface  $S_r$  of the sphere  $\Omega_r$  with radius  $r$  and center at  $(x, y)$ . The divergence of a vector field at point  $(x, y)$  is equal to the flux across the point divided by the volume of the sphere  $V_r$  as  $r$  approaches 0.

The physical meaning of this divergence operator is as follows. Since the divergence measures the flux across a point, it will be positive if the vector field at the point is expanding. Otherwise, the divergence will be negative. If there is no change in the vector field at the point, the divergence will be zero. Fig. 1(a) shows an expanding vector field and each vector has the same magnitude but different directions. Fig. 1(b) shows another example of an expanding vector field. Fig. 1(c) shows an example of a constant vector field, where each vector has the same magnitude and the same direction. Fig. 1(d) shows an example of a contracting vector field, where the magnitudes of the vectors are decreasing.

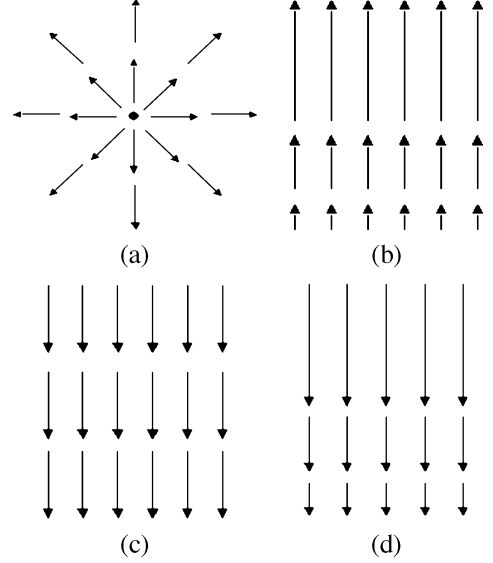


Fig. 1. Illustrations of the divergence of vector fields. (a) Expanding vector field. Each vector has the same magnitude. (b) Expanding vector field. (c) Constant vector field. (d) Contracting vector field.

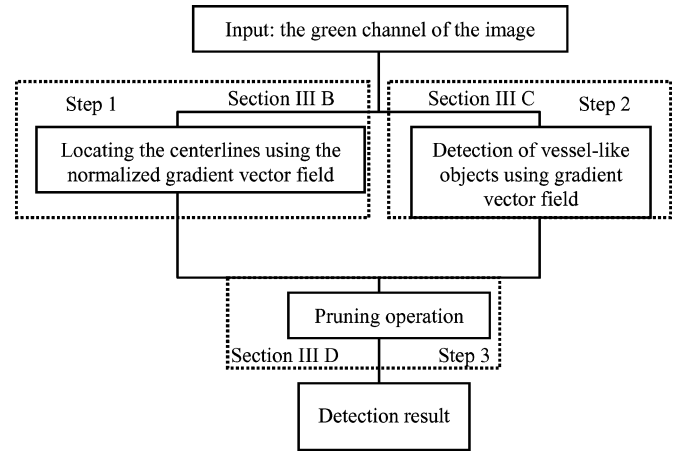


Fig. 2. Flow chart of the proposed method.

## III. ALGORITHM DESIGN

### A. Outline of the Proposed Method

In the proposed method, blood vessel-like objects are extracted using the Laplacian operator and noisy objects are pruned according to the centerlines, which are detected using the normalized gradient vector field. The method consists of three main steps illustrated in the flow chart shown in Fig. 2. The implementation details of the method will be given in Section IV.

### B. Locating the Centerlines Using the Normalized Gradient Vector Field

We use the normalized gradient vector field to locate the centerlines. As each pixel in the vector field has the same unit magnitude, the sign of the divergence depends only on the direction. A blood vessel is always darker than its neighborhood and thus, has a concave shape. Its normalized gradient vector field is expanding. This is similar to the example shown in Fig. 1(a).

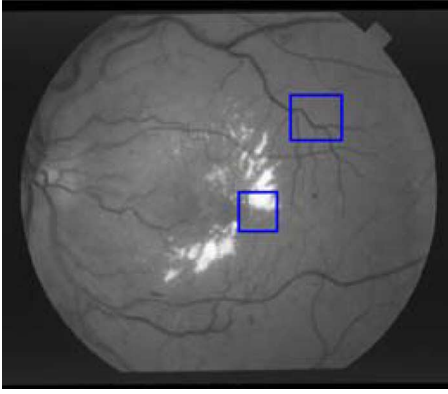


Fig. 3. Pathological retina image (Im0001).

Thus, we can locate a vessel by checking whether the pixel's divergence is positive. Fig. 3 shows a retinal image and Fig. 4(a) shows an example of blood vessels in a healthy region located in the upper right box in Fig. 3. The corresponding vector fields are shown in Fig. 4(b) and (c). The vectors point outwards inside the vessel and thus the corresponding pixels have positive divergence.

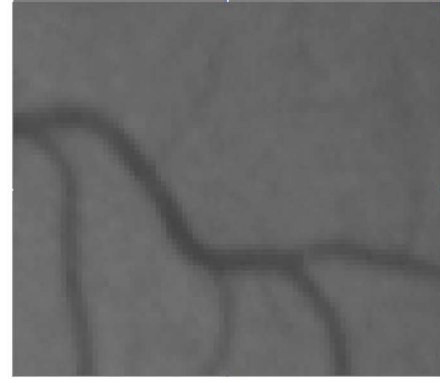
Fig. 5(a) shows a pathological region with bright abnormality in the center box in Fig. 3, while Fig. 5(b) shows the boundary of this region. Fig. 5(c) is the corresponding normalized gradient vector field. As the pathological region is brighter than its neighborhood, it has a convex shape and a negative divergence. Although positive divergence may be found in a group of noisy pixels in the vector field outside the vessel, they can be eliminated easily by the artifact removal scheme based on the connectivity of the vessels. Fig. 6 shows the detection result. We can see that no vessels are detected in the pathological region.

#### C. Detection of Blood Vessel-Like Objects Using Gradient Vector Field

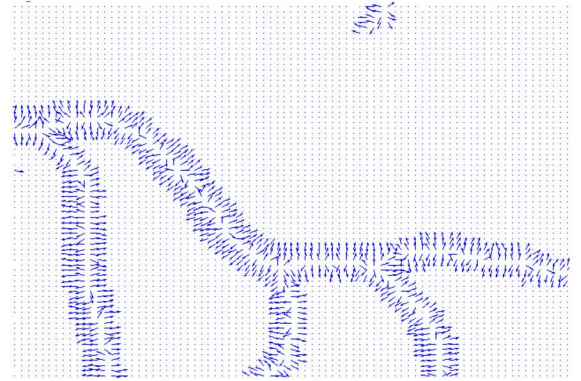
The goal of this step is to detect the blood vessel-like objects using the gradient vector field. As the vector field does not have the same magnitude of change in every direction, the sign of the divergence does not only depend on the orientation but also on the magnitude. This is similar to the situation shown in Fig. 1(b). Fig. 7 shows a healthy region and its corresponding gradient vector field. We can see that the vessels in the healthy region are expanding. By locating the pixel with positive divergence, the detection result can be obtained. The result after this step is shown in Fig. 8. We can see that almost all the vessel-like objects are detected successfully.

#### D. Pruning Operation

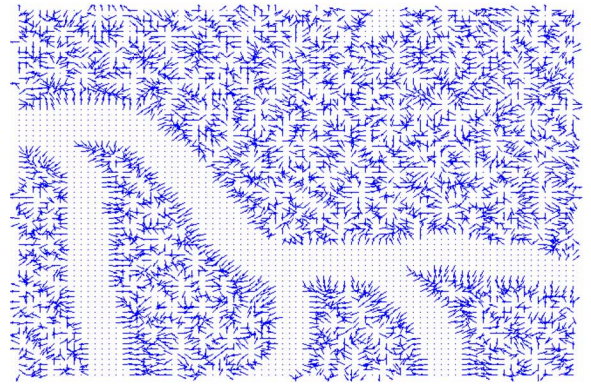
In this step, a pruning operation is carried out. The spurious detected blood vessel-like objects, as illustrated in Fig. 8, are pruned according to the detected centerlines. The key idea is to remove a pixel from the vessel-like objects if this pixel is far away from the centerline. Fig. 9 shows the result after this step for the image in Fig. 8. We can see that the falsely detected vessels near the pathological region are removed successfully.



(a)



(b)



(c)

Fig. 4. Blood vessels in a healthy region and their normalized gradient vector field. (a) Blood vessels in a healthy region, the upper right box in Fig. 3. (b) Normalized gradient vector field inside the vessels. (c) Normalized gradient vector field outside the vessels.

## IV. IMPLEMENTATION DETAILS

In this section, we explain the implementation details for the proposed method.

#### A. Computation of Divergence Values and Artifact Removal

Due to the presence of reflection on the tiny uneven surface of the soft tissue, some vessels have a large divergence value in some directions while the values in other directions are very small. These vessels can be detected more effectively by considering the divergence values under different smoothness and orientations. The procedure is given below. For a given input image

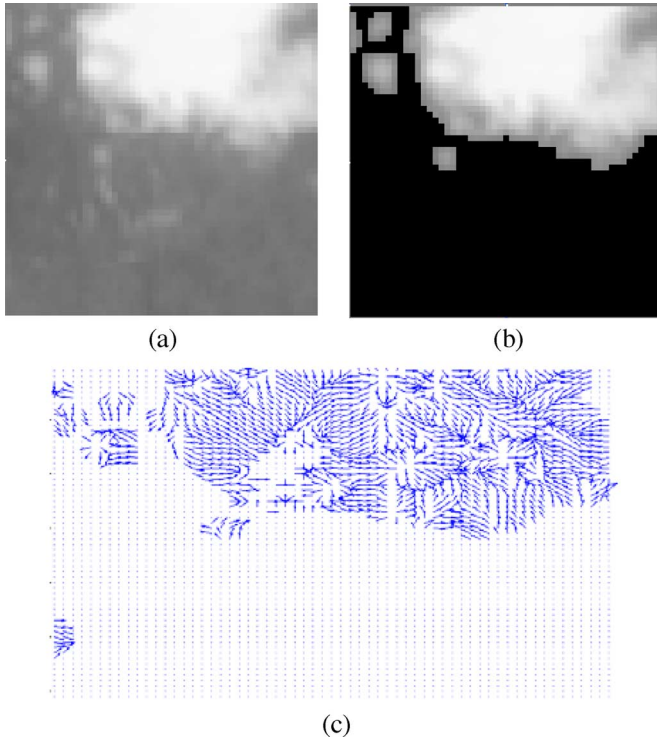


Fig. 5. Pathological region and its normalized gradient vector field. (a) Pathological region, the center box in Fig. 3. (b) Boundary of the pathological region. (c) Normalized gradient vector field of the region.

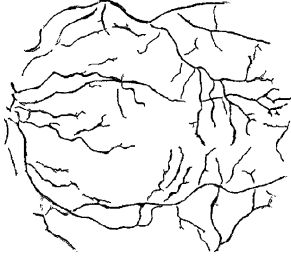


Fig. 6. Detected centerlines of the image in Fig. 3.

$I$ , we apply a Gaussian filter with fixed window size 41 and variance  $\sigma^2$  to the image. Then, we apply a horizontal and vertical edge detector to obtain the vector field  $F$ . A rotation matrix with angle  $\theta$  is applied to this vector field. After that, the divergence is computed by the summation of the two components, and the horizontal edge detector is applied to the  $x$ -component and vertical edge detector is applied to the  $y$ -component of the vector field  $F$  followed by the rotation matrix. This is the computation for the divergence value of the image  $I$  using the gradient vector field and we denote it as  $G(\theta, \sigma^2)$ . Here,  $G(\theta, \sigma^2)$  is also known as the oriented Laplacian. The same procedure (shown above) is used for the normalized gradient vector field, except that normalization is applied to the vector field  $F$  so that each pixel shares the same unit magnitude. We denote this divergence value as  $NG(\theta, \sigma^2)$ .

In order to remove artifacts in each processing step, we measure the length (in pixels) of the skeleton in each connected region. Skeletonization is conducted using the morphological operator [25]. The connected region is formed by four-connect-

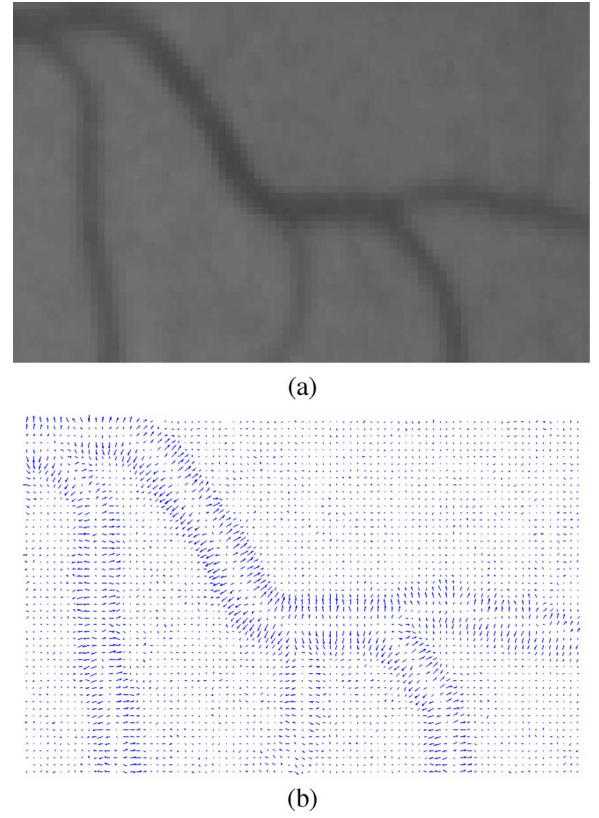


Fig. 7. Illustration of the divergence of the gradient vector for a blood vessel image. (a) Example of blood vessels. (b) Gradient vector field.

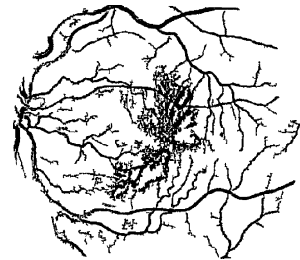


Fig. 8. Detected vessel-like objects.

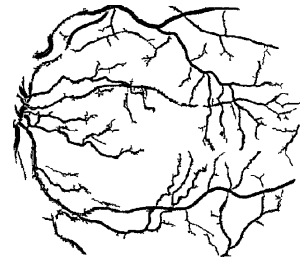


Fig. 9. Detection result after the pruning operation applied to the image in Fig. 8.

edness. In removal of artifacts, each connected region with a skeleton's length smaller than  $\delta = 50$  is removed. Here,  $\delta$  is a user-defined threshold constraining the length of the skeleton. A similar technique is adopted by Vermeer *et al.* [26]. They use  $\delta = 20$  to  $\delta = 40$  for artifact removal. In our experiments,

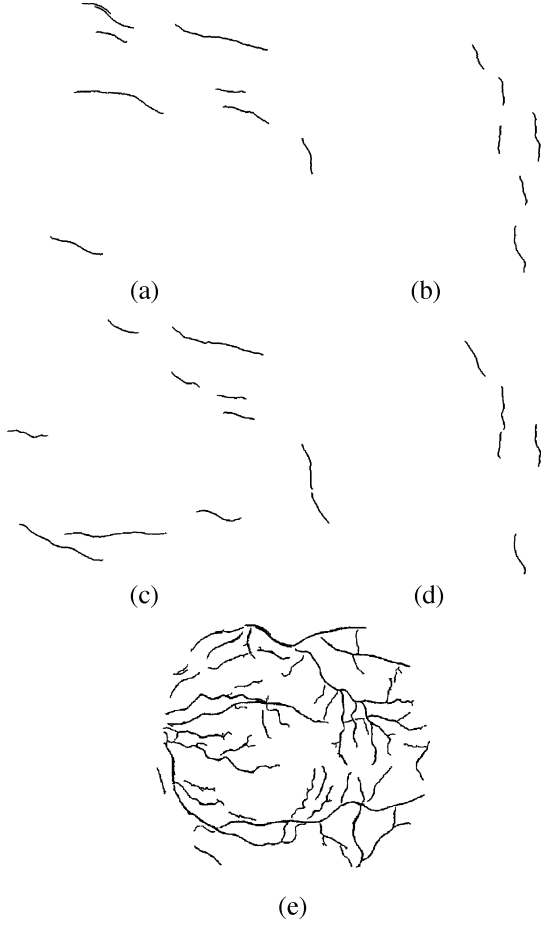


Fig. 10. Detected high-contrast centerlines. (a) Detected centerlines using  $\theta = 45^\circ$  and  $\sigma = 0.2$ . (b) Detected centerlines using  $\theta = 145^\circ$  and  $\sigma = 0.2$ . (c) Detected centerlines using  $\theta = 45^\circ$  and  $\sigma = 3$ . (d) Detected centerlines using  $\theta = 145^\circ$  and  $\sigma = 3$ . (e) Combining all the detected results.

$\delta = 50$  is taken and a perturbation to this value yields almost the same result.

### B. Locating the Centerlines Using the Normalized Gradient Vector Field

The normalized gradient vector field  $NG(\theta, \sigma^2)$  is used to detect the centerlines. This step consists of two different phases: detecting the high-contrast and the low-contrast centerlines. The high-contrast centerlines refer to the vessels in the region with high foreground and background contrast, such as those placed at the middle of the image. The low-contrast centerlines refer to the vessels in the region with low contrast, such as those placed near the boundary of the field-of-view (FOV) of the image. In each of these phases, the whole image domain is considered as an input. For detecting the high-contrast centerlines, the smoothness parameter  $\sigma^2$  from 0 to 4 with interval 0.2 and the rotation parameter  $\theta$  from 0 to  $\pi$  with interval  $\pi/36$  are used. For each pair  $(\theta, \sigma^2)$ , a pixel having a divergence value of  $NG(\theta, \sigma^2) > \phi_1$  which passes the artifact removal scheme is a candidate for the centerline. Here,  $\phi_1$  is a user-defined parameter. Its selection will be discussed in Section V. Based on these parameter settings, the algorithm produces 100 centerline results in total in Fig. 10. By combining all the results, we obtain the high-contrast centerlines. The combination is the union

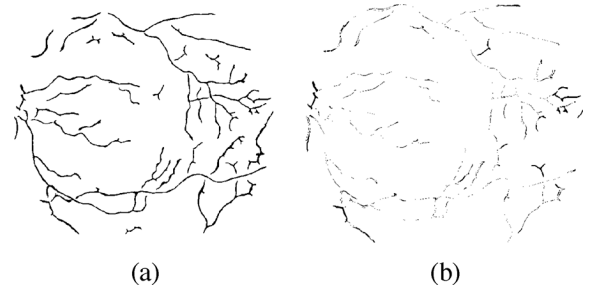


Fig. 11. Low-contrast centerlines. (a) Detected low-contrast centerlines. (b) Extra number of detected low-contrast pixels.

of all these results. Fig. 10(a)–(d) shows the results using different pairs of  $(\theta, \sigma^2)$  and Fig. 10(e) shows the high-contrast centerlines. We can see that vessels are detected successfully.

For detecting the low-contrast centerlines, no rotation is applied and the parameter  $\theta$  is set to zero. Two ranges for smoothness parameter  $\sigma^2$  are taken. In the first range,  $\sigma^2$  is 3 to 4 with interval 0.2, while in the second range,  $\sigma^2$  is 4 to 5 with interval 0.2. We use large smoothness parameters here because the contrast in this kind of centerlines is low and small smoothness parameters may produce many artifacts. The rule, which determines a candidate of the centerline, is given below

$$\max_{\sigma} \left\{ \frac{NG(0, \sigma^2)}{G(\sigma^2) \otimes I/255} \right\} > \phi_2 \quad (2)$$

where  $G(\sigma^2)$  represents the Gaussian filter with smoothness parameter  $\sigma^2$ , and  $\otimes$  is the convolution operator.  $\phi_2$  is a user-defined parameter and will be defined in Section V. In each range, a pixel satisfying (2) passing the artifact removal scheme is a candidate for a centerline. By combining the results from these two ranges, the low-contrast centerlines (Fig. 11) are obtained. We can see that the vessels placed near the edge of the FOV can be detected successfully.

The centerlines of the retinal image are obtained by combining the low-contrast centerlines and the high-contrast centerlines. In the low-contrast centerlines, long line-shaped artifacts can be produced using large smoothing parameters. We use the following strategy to prune these artifacts. If a segment of any low-contrast centerline is not close to any high-contrast centerline, it will be pruned. Here, the low-contrast centerlines are first separated into four-connected regions. If the region has a 40% intersection with the high-contrast centerlines, it is merged with the high-contrast centerlines. Fig. 11(b) shows the extra number of detected pixels compared with the high-contrast centerlines after this step.

### C. Detection of Blood Vessel-Like Objects Using the Gradient Vector Field

The gradient vector field  $G(\theta, \sigma^2)$  is used in this step to detect the blood vessel-like objects. The range for  $\sigma^2$  is from 0 to 4 with interval 0.2. Two rotation parameters are  $0^\circ$  and  $45^\circ$

$$\frac{G(\theta, \sigma^2)}{G(\sigma^2) \otimes I/255} > \phi_3. \quad (3)$$

For each pair  $(\theta, \sigma^2)$ , a pixel satisfying (3) and passing the artifact removal scheme is a candidate for the vessel-like objects.  $\phi_3$



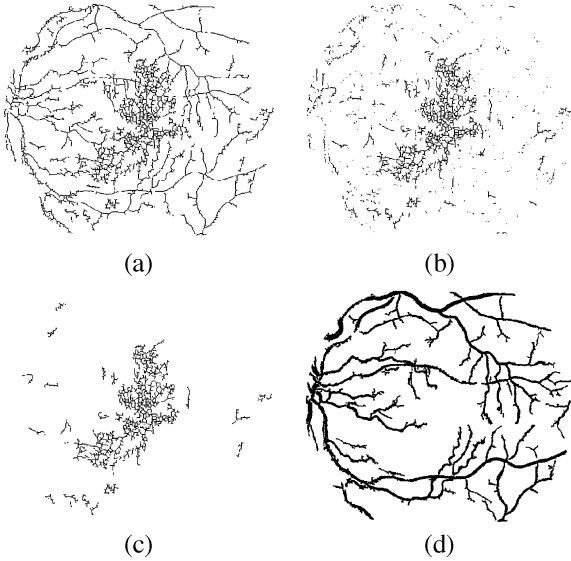


Fig. 12. Pruning operation. (a) Skeleton of the vessel-like object. (b) Skeleton belonging to the second group. (c) Artifacts removed. (d) Detection result.

is a user-defined parameter and will be defined in Section V. By combining all the results, the vessel-like objects are obtained. Fig. 8 shows the result of this step.

#### D. Pruning Operation

After detecting the blood vessel-like objects in the image, the spurious objects are pruned according to the detected centerlines so that the falsely detected vessels near the pathological region can be removed. The procedure is given below. They are first converted into its skeleton form using a morphological operator [25]. The vessel-like objects are then classified into two groups. The first group contains pixels closer, or having equal distance, to the centerlines and the second group contains pixels closer to the skeleton. The artifact removal scheme with eight connected regions is applied to the second group and the pixels passing this scheme are pruned. These pruned pixels are merged back to the centerlines to form the detection result. Fig. 12(a) shows the skeleton of the vessel-like objects and Fig. 12(b) the group far away from the centerlines. Fig. 12(c) shows the artifacts removed, and Fig. 12(d) the detection result.

### V. EXPERIMENT EVALUATION

#### A. Databases

We use all the pathological retina images in the STARE database<sup>1</sup> to evaluate the proposed method and compare its performances with other methods. The performances on the DRIVE database<sup>2</sup> are given in the supplementary materials as reference. The reasons for using the STARE database for evaluation is that it is available publicly and the reader can download the database on the website. Also, several difficult pathological retina images can be found in this database.

<sup>1</sup><http://www.parl.clemson.edu/stare/probing/>

<sup>2</sup><http://www.isi.uu.nl/Research/Databases/DRIVE/>

We use three different measures to evaluate the performance of the methods. They are the overall accuracy, receiver operating characteristic (ROC) curve and the accuracy in the pathological region. Accuracy for a retinal image with a given set of parameters  $k$  is defined as the number of true positive vessel pixels plus the number of true positive background pixels divided by the total number of pixels in the FOV. The FOV is the region of the retina while the region not in the FOV is the background of the retinal image, which is usually dark. As the dark background outside the FOV can be easily detected, all the measurements are carried out inside the FOV. In this paper, the accuracy for the pathological retina images in the STARE database is taken as the maximum of the average accuracy for all the images in the database with respect to the parameter  $k$ . In the ROC curve, the two axes are the true positive fraction (tpf) for the vertical axis, and the false positive fraction (fpf) for the horizontal axis [27], [28]. The closer the curve approaches the top left hand corner, the better the performance of the method. A common single measure to quantify the performance of the method is to compute the area under the curve  $R_{\text{area}}$ . An area close to one means a good performance. In this paper, the tpf and fpf values are computed by varying the parameters of the algorithm. Then, the  $R_{\text{area}}$  is approximated by adding (0, 0) and (1,1). In this database, we employ the first observer's manual segmentation as ground truth for evaluation. The second observer's (tpf, fpf) are plotted on the ROC graph. In addition to the classification accuracy and the ROC curve, we also propose a new measure to evaluate the performance in the pathological region (PUR) of a detection method. This measure is similar to accuracy, but it puts the emphasis on pathological regions that are especially important but difficult to deal with. The PUR is defined as the number of true positive pixels plus the number of true positive background pixels that are at least  $T$  pixels away from the true positive blood vessels pixels, divided by the total number of pixels involved. As a pathological region is near the true positive background pixels and somewhat away from the true positive vessels pixels, a large PUR means that the method is less sensitive to the presence of the pathological region with respect to the parameter  $T$ . In this paper,  $T$  varies from 0 to 25 pixels. If  $T$  is equal to zero, all the pixels in the whole retina image are taken into account for computation. If  $T$  is large, only the pixels, which are far away from the true vessels, are considered in the true positive background pixels. It is noticed that the true positive fraction is independent of the choice of the parameter  $T$ . For convenience, we use  $\text{PUR}(T, k)$  to denote the PUR measure for different  $T$  values and parameter setting  $k$ .

#### B. Parameter Settings

The input image is obtained from the green channel of the image, which contains the richest information on the blood vessels [3], [8]. For the proposed method, tpf and fpf are set to the following values:  $\phi_1 = 0.4 + 0.05(k - 1)$ ,  $\phi_2 = 1$  and  $\phi_3 = 1 + 0.5(k - 1)$  for  $k = -1, \dots, 6$ . Under this setting, the proposed method requires about 25 min to produce the detection results for a single retinal image. We use MATLAB to implement our method on a computer with Intel Pentium 2.66 GHz and 512 MB RAM. The algorithms can be optimized

TABLE I  
PARAMETERS FOR JIANG AND MOJON'S METHOD

$P_\phi$	$(150 - 5k)\pi/180$
$P_d$	$6 + k$
$P_{fac}$	2
$P_{contrast}$	1.07
$P_{size}$	$46 - 3k$
Range	$k = 0, \dots, 7$

TABLE II  
PARAMETERS FOR VERMEER *et al.*'S METHOD

$\sigma$ (Laplace)	$\sigma + (-1.5 + 0.5k)$
$\theta_{lo}$	$\theta_{lo} + (0.05 + 0.05k)$
$\sigma$ (contrast)	$6 + k$
Min. skeleton length	$20 + 3k$
Range	$k = 0, \dots, 9$

TABLE III  
RESULTS FOR THE STARE DATABASE USING DIFFERENT METHODS

STARE	Accuracy	$R_{area}$
Vermeer <i>et al.</i>	0.9287	0.9187
Jiang and Mojon	0.9337	0.8906
Soares <i>et al.</i> (DRIVE)	0.9428	0.9455
Soares <i>et al.</i> (STARE)	0.9425	0.9571
Proposed	0.9474	0.9392
2nd Observer	0.9410	N/A

and speeded up using other programming languages, such as C. We compare the performance of the proposed method with two unsupervised learning methods and two different results of a supervised learning method. We implement the two unsupervised methods, which are the adaptive thresholding technique by Jiang and Mojon [2] and the model-based technique by Vermeer *et al.* [26]. The parameters for these two methods are shown in the Tables I and II. The values of tpf and fpf are obtained by experiments so that the optimal  $R_{area}$  is reached. Also, one step of Vermeer *et al.* method conducts pruning with the aid of human visual assessment [26, Sec. III-B]. As this step is very subjective, we have only carried out a major clean up of the detection results along the boundary of the FOV so that maximum accuracy can be reached. This procedure is not applied to the proposed method or the method of Jiang and Mojon. For the supervised method, we use the method proposed by Soares *et al.* Their results are available on the website.<sup>3</sup> We use the two results from the classifier with 20 Gaussian models trained by the STARE and the DRIVE databases, which produce the best results in their paper. The reason for comparing the results obtained from training the DRIVE database to detect vessels in the STARE database is that the ground truth labels for a database may not be available in real applications. We can only use existing databases to train the classifier for blood vessel segmentation.

<sup>3</sup><http://www.retina.iv.fapesp.br>

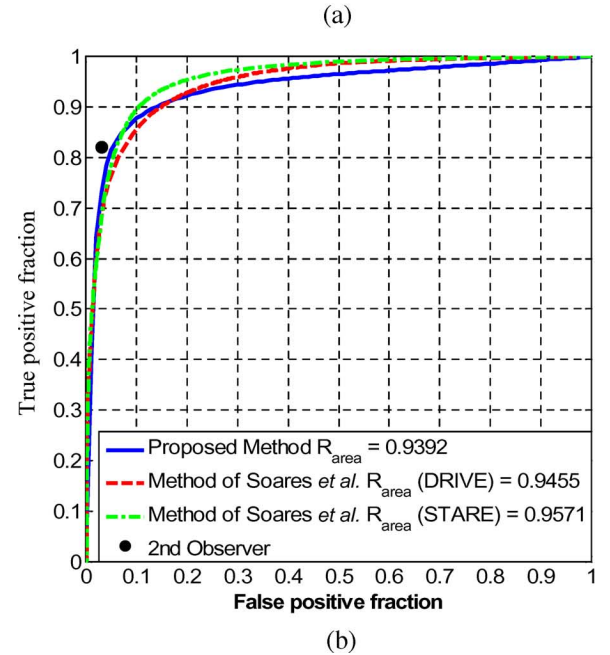
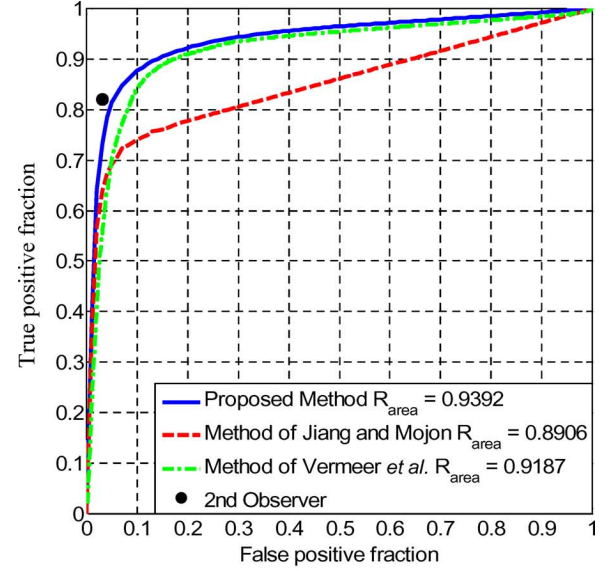


Fig. 13. ROC curves for the pathological retina images in the STARE database. Comparing the second observer to the first observer, true and false positive fractions of (0.8215, 0.0307) are found. (a) ROC curves of the proposed method and the two unsupervised methods. (b) ROC curves of the proposed method and the two results by the supervised method.

### C. Results

The evaluation measures using the overall accuracy and  $R_{area}$  values are given in Table III. In this table, we can see that the proposed method has a better performance than both supervised and unsupervised methods in accuracy.

Fig. 13(a) shows the ROC curves of the proposed method and the two unsupervised methods. We can see that the curve for the proposed method is completely above the two other curves and yields the largest  $R_{area}$  value. Fig. 13(b) shows the ROC curves of the proposed method and the results using the supervised learning method. In this figure, we can see that the ROC curve from the proposed method is not completely above the curve from the two results of Soares *et al.* except in the initial part of

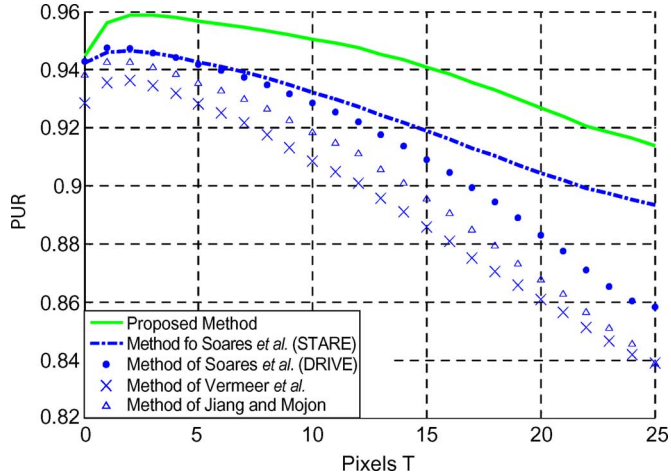


Fig. 14. Performance evaluation measure PUR for different methods using all the pathological images.

the curve. The main reason for the proposed method having a smaller  $R_{\text{area}}$  and part of its initial ROC curve below the supervised method is given as follows. As discussed in the introductory section, the supervised method learns from human-labeled data and it is able to yield accurate results near the edge of the ground truth region. Thus, in the ROC curves, an increase in the true positive fraction does not lead to a large increase in the false positive fraction and the supervised method is able to yield a larger  $R_{\text{area}}$  value. In contrast to the supervised method, the proposed method is more robust to the pathological regions and can avoid detecting false vessels in these regions. It is able to yield a solution very similar to the ground truth. Thus, it produces the highest accuracy among others, including the supervised method, and yields a ROC curve closest to the pair (fpf, tpf) from the second observer for the pathological images.

We also use the third evaluation measure to verify the robustness of the methods for pathological regions. Fig. 14 shows the PUR of all the pathological images using different methods. The  $x$  axis represents the number of pixels  $T$  used in computing PUR and the  $y$ -axis refers to the PUR. The way to select the parameter set  $k$  is as follows. For a given pixel distance parameter  $T$ , the optimal value of  $k$ , denoted as  $k^*$ , is found by maximizing the average  $\text{PUR}(T, k)$  for all the images. The entire range of  $k$  for the two unsupervised methods and the supervised method are used as the search space. For the proposed method, a smaller range,  $k = 3$  to  $5$  is used. The reason for the restriction is to show the robustness of the proposed method compared to other methods under different parameter settings. Fig. 14 shows that the proposed method has the highest PUR from  $T = 0$  to  $T = 25$ . When  $T$  is near zero,  $\text{PUR}(T, k)$ , using different methods, shares almost the same value. However, when  $T$  increases, the proposed method yields a higher accuracy than others and their difference becomes larger. As a pathological region is near the true positive background pixels and somewhat away from the true positive blood vessel pixels, the PUR value for changing  $T$  shows the accuracy of a method towards the pathological region. This means that the proposed method is more robust than other methods in pathological regions.

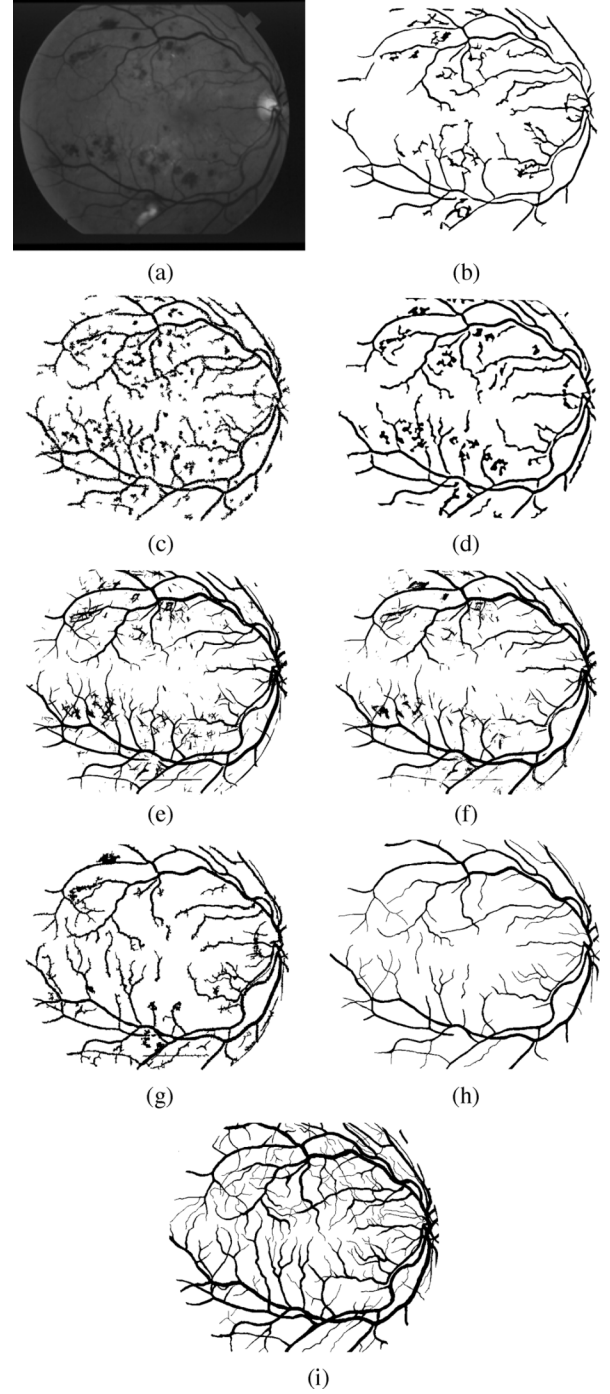


Fig. 15. Results for a pathological retina image with a dark abnormality obtained using different methods. (a) Retinal image with dark abnormality (Im0139). (b) Hoover *et al.* (tpf, fpf) = (0.6660, 0.0499). (c) Jiang and Mojon (tpf, fpf) = (0.9009, 0.1245). (d) Vermeer *et al.*; (tpf, fpf) = (0.8626, 0.0949). (e) Soares *et al.* (DRIVE) (tpf, fpf) = (0.8966, 0.0868). (f) Soares *et al.* (STARE) (tpf, fpf) = (0.8981, 0.0640). (g) Proposed method. (tpf, fpf) = (0.8935, 0.0839). (h) Ground truth 1. (i) Ground truth 2.

## VI. DISCUSSION AND CONCLUSION

Detecting blood vessels in a pathological retina image is a challenging problem. In our proposed method, we solve this problem by detecting the blood vessel-like objects in the image using the Laplacian operator and the noisy objects are pruned



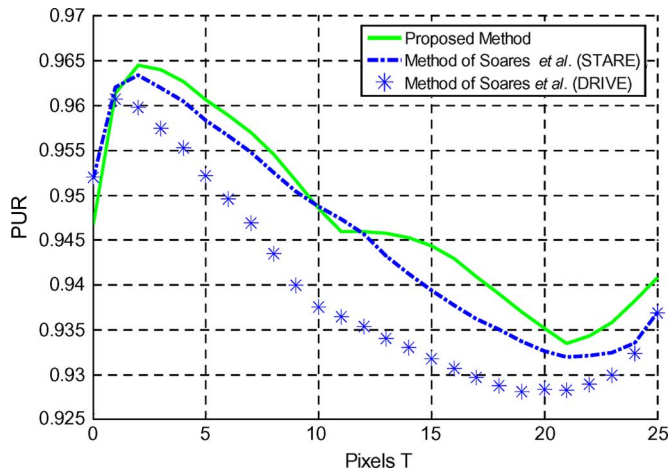


Fig. 16. Performance evaluation in the pathological region of the retinal image (Im0139).

according to the detected centerlines, which are extracted using the normalized gradient vector field. Experiment results show that our method is able to yield an accurate result especially for pathological retina images.

#### A. Limitation of the Proposed Method

In this paper, we focus our discussion on bright abnormality. Dark abnormality is also present in a pathological retina image. Fig. 15(a) is an example. Fig. 15(b)–(g) shows the results using different methods. Fig. 15(h) and (i) shows the ground truths obtained by two different human observers. There is a remarkable difference between the two ground truths. The reason is that the pixel values are small compared with other retinal images. For human vision, a different conclusion can be made as to whether a pixel belongs to a vessel or a nonvessel, in a dark region with a tiny uneven surface. Fig. 15(c) shows the result using the method of Jiang and Mojon and several dots are apparent. The reason for the spots is given below. The detection is conducted under different intensity levels. If an abnormal region of large size exists in one of these levels, then this region cannot be pruned by the algorithm and thus becomes part of the detection results. Fig. 15(e) and (f) show the results obtained using the method of Soares *et al.* There are more spots detected near the vessels using Soares *et al.* (DRIVE). This is because a different training image set is used for the results of Soares *et al.* (DRIVE), which can degrade the performance. The result obtained using the proposed method is shown in Fig. 15(g). We can see that it is able to detect many short vessels without producing many spots near the pathological region. However, if a dark abnormality is very close to a vessel, an artifact can still be formed.

Now, we compare the performance of the proposed method and the method of Soares *et al.* near the pathological region using the PUR measure. This is shown in Fig. 16. We can see that the proposed method generally has a better performance than Soares *et al.* This implies that the performance of the proposed method is still better than the supervised method in the pathological region with a dark abnormality.

#### B. Future Work

Although the proposed method shows a good performance for pathological images, there is still room for further improvement. In Section VI-A, it is shown that the proposed method shows a better performance than other methods for the pathological retina image having dark abnormality. However, several spots are falsely detected as vessels. In the future, we may be able to use other features to resolve this problem. One possible solution is to prune the vessel-like objects having spherical shape, as the false detected vessels appear in this form.

Another improvement that can be made with the proposed method is the performance near blood vessel edges. Although the supervised method has limitations for pathological regions, it produces good results near blood vessel edges. In future, we can combine the proposed method and the supervised method to yield overall better results.

#### ACKNOWLEDGMENT

The authors would like to thank J. J. Staal and A. Hoover for making their databases publicly available. Also, the suggestions and comments of anonymous reviewers, which have greatly helped to improve the quality of this paper, are acknowledged.

#### REFERENCES

- [1] S. Chaudhuri, S. Chatterjee, N. Katz, M. Nelson, and M. Goldbaum, "Detection of blood vessels in retinal images using two-dimensional matched filters," *IEEE Trans. Med. Imag.*, no. 3, pp. 263–269, Sep. 1989.
- [2] X. Jiang and D. Mojon, "Adaptive local thresholding by verification-based multithreshold probing with application to vessel detection in retinal images," *IEEE Trans. Pattern Anal. Mach. Intell.*, vol. 25, no. 1, pp. 131–137, Jan. 2003.
- [3] J. J. Staal, M. D. Abramoff, M. Niemeijer, M. A. Viergever, and B. van Ginneken, "Ridge based vessel segmentation in color images of the retina," *IEEE Trans. Med. Imag.*, vol. 23, no. 4, pp. 501–509, Apr. 2004.
- [4] J. V. B. Soares, J. J. G. Leandro, R. M. Cesar, Jr., H. F. Jelinek, and M. J. Cree, "Retinal vessel segmentation using the 2-D gabor wavelet and supervised classification," *IEEE Trans. Med. Imag.*, vol. 25, no. 9, pp. 1214–1222, Sep. 2006.
- [5] T. Chanwimaluang and F. Guoliang, "An efficient blood vessel detection algorithm for retinal images using local entropy thresholding," in *Proc. 2003 Int. Symp. Circuits Syst.*, 2003, vol. 5, pp. 21–24.
- [6] A. Hoover, V. Kouznetsova, and M. Goldbaum, "Locating blood vessels in retinal images by piece-wise threshold probing of a matched filter response," *IEEE Trans. Med. Imag.*, vol. 19, no. 3, pp. 203–210, Mar. 2000.
- [7] A. Pinz, S. Bernogger, P. Datlinger, and A. Kruger, "Mapping the human retina," *IEEE Trans. Med. Imag.*, vol. 17, no. 4, pp. 606–619, Apr. 1998.
- [8] Y. A. Tolias and S. M. Panas, "A fuzzy vessel tracking algorithm for retinal images based on fuzzy clustering," *IEEE Trans. Med. Imag.*, vol. 17, no. 2, pp. 263–273, Apr. 1998.
- [9] A. K. Klein, L. Forester, and A. A. Amini, "Quantitative coronary angiography with deformable spline models," *IEEE Trans. Med. Imag.*, vol. 16, no. 5, pp. 468–482, Oct. 1997.
- [10] S. R. Fleagle, M. R. Johnson, C. J. Wilbricht, D. J. Skorton, R. F. Wilson, C. W. White, M. L. Marcus, and S. M. Collins, "Automated analysis of coronary arterial morphology in cineangiograms: Geometric and physiological validation in humans," *IEEE Trans. Med. Imag.*, vol. 8, no. 4, pp. 387–400, Dec. 1989.
- [11] S. Tamura, Y. Okamoto, and K. Yanashima, "Zero-crossing interval correction in tracing eye-fundus blood vessels," *Pattern Recognit.*, vol. 21, pp. 227–233, 1988.

- [12] M. Figueiredo and J. Leitaó, "A nonsmoothing approach to the estimation of vessel contours in angiograms," *IEEE Trans. Med. Imag.*, vol. 14, pp. 162–172, 1995.
- [13] A. Hoover and M. Goldbaum, "Locating the optic nerve in a retinal image using the fuzzy convergence of the blood vessels," *IEEE Trans. Med. Imag.*, vol. 22, no. 8, pp. 951–958, Aug. 2003.
- [14] M. Sofka and C. V. Stewart, "Retinal vessel centerline extraction using multiscale matched filters, confidence and edge measures," *IEEE Trans. Med. Imag.*, vol. 25, no. 12, pp. 1531–1546, Dec. 2006.
- [15] M. Sofka and C. V. Stewart, "Erratum to "retinal vessel centerline extraction using multiscale matched filters, confidence and edge measures"," *IEEE Trans. Med. Imag.*, vol. 26, no. 1, pp. 133–133, Jan. 2007.
- [16] B. S. Y. Lam and H. Yan, "Blood vessel extraction based on Mumford-Shah model and skeletonization," in *Int. Conf. Mach. Learn. Cybernetics*, 2006, pp. 4227–4230.
- [17] S. Esedoglu and J. Shen, "Digital inpainting based on the Mumford-Shah-Euler image model," *Eur. J. Appl. Math.*, vol. 13, pp. 353–370, 2002.
- [18] T. Chan and J. Shen, *Image processing and analysis: variational, PDE, wavelet, and stochastic methods*. Philadelphia, PA: Soc. Indust. Appl. Math., 2005.
- [19] T. Chan, S. Osher, and J. Shen, "The digital TV filter and nonlinear denoising," *IEEE Trans. Image Process.*, vol. 10, no. 2, pp. 231–241, Feb. 2001.
- [20] J. A. Sethian, *Level Set Methods: Evolving Interfaces in Geometry, Fluid Mechanics, Computer Vision and Materials Sciences*. Cambridge, U.K.: Cambridge Univ. Press, 1996.
- [21] S. Osher and R. Fedkiw, *Level Sets Methods and Dynamic Implicit Surfaces*. New York: Springer, 2003.
- [22] G. K. Batchelor, *An Introduction to Fluid Dynamics*, 1st ed. Cambridge, U.K.: Cambridge Univ. Press, 2000.
- [23] D. J. Griffiths, *Introduction to Electrodynamics*, 3rd ed. Upper Saddle River, NJ: Prentice Hall, 1999.
- [24] W. Kaplan, *Advanced Calculus*, 4th ed. Reading, MA: Addison-Wesley, 1991.
- [25] K. R. Castleman, *Digital Image Processing*. Englewood Cliffs, N.J.: Prentice-Hall, 1979.
- [26] K. A. Vermeer, F. M. Vos, H. G. Lemij, and A. M. Vossepoel, "A model based method for retinal blood vessel detection," *Computers Biol. Med.*, vol. 34, pp. 209–219, 2004.
- [27] P. Armitage and T. Colton, "Receiver operating characteristic (ROC) curves," in *Encyclopedia of Biostatistics*. New York: Wiley, 1998, pp. 3738–3745.
- [28] N. A. Obuchowski, "Receiver operating characteristic curves and their use in radiology," *Radiology*, vol. 229, pp. 3–8, 2003.